



# Earthquake alerting based on spatial geodetic data by spatiotemporal information transformation learning

Yuyan Tong<sup>a</sup> , Renhao Hong<sup>a</sup>, Ze Zhang<sup>b</sup> , Kazuyuki Aihara<sup>c</sup> , Pei Chen<sup>a,1</sup> , Rui Liu<sup>a,1</sup> , and Luonan Chen<sup>b,d,e,f,1</sup>

Edited by Peter Kelemen, Lamont-Doherty Earth Observatory, Palisades, NY; received February 18, 2023; accepted June 7, 2023

Alerting for imminent earthquakes is particularly challenging due to the high nonlinearity and nonstationarity of geodynamical phenomena. In this study, based on spatiotemporal information (STI) transformation for high-dimensional real-time data, we developed a model-free framework, i.e., real-time spatiotemporal information transformation learning (RSIT), for extending the nonlinear and nonstationary time series. Specifically, by transforming high-dimensional information of the global navigation satellite system into one-dimensional dynamics via the STI strategy, RSIT efficiently utilizes two criteria of the transformed one-dimensional dynamics, i.e., unpredictability and instability. Such two criteria contemporaneously signal a potential critical transition of the geodynamical system, thereby providing early-warning signals of possible upcoming earthquakes. RSIT explores both the spatial and temporal dynamics of real-world data on the basis of a solid theoretical background in nonlinear dynamics and delay-embedding theory. The effectiveness of RSIT was demonstrated on geodynamical data of recent earthquakes from a number of regions across at least 4 y and through further comparison with existing methods.

spatiotemporal information transformation learning | earthquake alerting | real-time geodynamic data | tipping point | delay-embedding theorem

Earthquakes are natural disasters that originate from the sudden and catastrophic release of slowly accumulated strain energy within the Earth's lithosphere. Many facts indicate that the dominant mechanism for the occurrences of catastrophic earthquakes is differential movements and interactions of active tectonic blocks (1). One of the largest earthquakes on record (with a magnitude of M9.0) struck Northeast Japan on March 11, 2011. This event generated a devastating tsunami that inundated the coastal areas of Tohoku, Kanto and southern Hokkaido, killing 15,848 people and triggering nuclear meltdowns in Fukushima. Such severe disasters have painfully emphasized the urgency and importance of alerting for possible catastrophic earthquakes, which is, however, notoriously difficult. Since the middle of the last century, the study about precursors of strong earthquakes has become an important and challenging task of modern geophysics (2). Some scholars have reported observing geological phenomena prior to earthquakes, indicating that the gradual accumulations of stress and strain in the Earth's lithosphere often result in abnormal physical and chemical changes in the area surrounding the epicenter (3). These changes related to strain buildup and earthquake occurrence are called earthquake precursors (3). Retrospective studies of various earthquake precursors have revealed anomalous trends before earthquakes (4), such as trends in subsoil radon gas emissions (5), total electron contents of the ionosphere (6), the Earth's electric and magnetic fields (6), deformations of the Earth's surface (7), and groundwater levels (8). Based on these precursor phenomena, many efforts have been devoted to detecting possible signals that may warn of an impending earthquake. For instance, some researchers measured the Earth's electric field under the assumption that some electric current may be generated in the seismogenic region before the event; however, they discovered that these preseismic signals exist only if the correct location (i.e., the area containing the seismic stations sensitive to the event) is chosen (9). Despite these observations, however, it remains challenging to alert for earthquakes due to the high nonlinearity, nonstationarity and complexity of the underlying geodynamics. Actually, from the perspective of nonlinear geophysics, the earth is a huge open system where there is the exchange of energy and mass among the blocks composing the system. During this process, the system would be unstable when the energy of some blocks reaches a certain amount, possibly resulting in the occurrence of earthquakes. Generally, the larger the size of an unstable block is, the higher the intensity of the earthquake becomes (10).

In particular, taking California as an example, approximately half of the large quakes are preceded by weaker foreshocks, but there is only a small probability (about 5%~7%) of an earthquake being a foreshock to a larger one (11–13). This inconsistent relation

## Significance

It is notoriously challenging to alert for earthquakes due to the high nonlinearity, nonstationarity, and complexity of the underlying geodynamics. Here, we developed an efficient computational method based on spatiotemporal information transformation for high-dimensional real-time data. From the perspectives of critical slowing down and delay embedding theory, such a method can identify local deformation precursors by detecting signals both from the unpredictability and instability of geodynamics and thus alert for possible earthquakes in a timely manner. With real-time spatial geodetic time-series data, the application of this method in various regions demonstrated its potential in alerting for strong earthquakes.

Author contributions: P.C., R.L., and L.C. designed research; Y.T., P.C., and R.L. performed research; Z.Z. contributed new reagents/analytic tools; Y.T. and R.H. analyzed data; and Y.T., R.H., K.A., P.C., R.L., and L.C. wrote the paper.

The authors declare no competing interest.

This article is a PNAS Direct Submission.

Copyright © 2023 the Author(s). Published by PNAS. This article is distributed under [Creative Commons Attribution-NonCommercial-NoDerivatives License 4.0 \(CC BY-NC-ND\)](https://creativecommons.org/licenses/by-nc-nd/4.0/).

Although PNAS asks authors to adhere to United Nations naming conventions for maps (<https://www.un.org/geospatial/mapsgeo>), our policy is to publish maps as provided by the authors.

<sup>1</sup>To whom correspondence may be addressed. Email: Inchen@sibs.ac.cn, scliruui@scut.edu.cn, or chenpei@scut.edu.cn.

This article contains supporting information online at <https://www.pnas.org/lookup/suppl/doi:10.1073/pnas.2302275120/-/DCSupplemental>.

Published September 5, 2023.

poses a dilemma; should an earthquake-warning system trigger an alarm for every large seismic event despite the risk of false positives, or compromise by sacrificing accuracy to decrease the number of false alarms? To provide warnings for as many severe earthquakes as possible while maintaining a low false-positive rate, a region-specific tradeoff is necessary.

To address this challenging task, deep learning methods have been applied to earthquake alert, and researchers have evaluated the performance of neural network techniques in predicting earthquakes (14). Data of event times, epicentral latitudes and longitudes, focal depths, and magnitudes were gathered to be converted into inputs for neural networks, and the results showed that a neural network method can achieve better warning accuracy for earthquakes with magnitudes of 3–5 than the methods in previous works (14); nevertheless, satisfied results could not be obtained for earthquakes with magnitudes of 5–8 due to the lack of sufficient data. Some studies attempted to alert for earthquakes by using time series of seismic electric signal data (6, 15). However, while most of these neural network methods use various kinds of features as inputs to predict the timing and/or magnitude of earthquakes, few of them consider the spatial relations such as surface deformations of multiple regions (16).

Surface deformations prior to earthquakes have garnered attention and interest from seismologists. Theoretical and laboratory results of rock deformation research before the fracture, especially the observation of dilatancy in rocks just prior to their fracture, suggest that in many cases, surface deformations could be observed (7), implying that some observable surface deformations occur prior to an earthquake. In addition, according to the numerous records of geophysical anomalies prior to earthquakes, deformation precursors, such as horizontal and vertical deformations of the earth's surface, occupy the largest proportion in terms of the recording frequency (2, 8). However, in the past, it has been time-consuming and laborious to observe or detect surface deformations (7). Recently, with the emergence of geodetic approaches and their rapid improvement over time, the early warning of earthquakes has entered a new phase (17). Fast and cost-effective geodetic technology, such as the global navigation satellite system (GNSS), has enabled the movements of the Earth's surface to be monitored in many locations simultaneously in real-time, yielding millimeter-scale observations of plate tectonics (18). Using these high-dimensional spatial geodetic observations of preseismic movements for (large) earthquakes, the risk of a catastrophic earthquake may be estimated more accurately than using either seismological or geological conventional approaches (17). Therefore, recent developments in geodetic techniques have provided the motivation to develop an efficient method to identify the local deformation precursors and thus alert for potential strong earthquakes in a timely and robust manner by fully exploring high-dimensional spatial geodetic time-series data.

From a dynamical systems viewpoint, we can represent the geodynamics of the Earth as a time-varying, high-dimensional dynamical system in which an earthquake can be viewed as a drastic state transition from one stable equilibrium to another caused by the gradual change in its time-varying seismic parameters. Thus, from the perspective of dynamical systems theory, an earthquake may be alerted from high-dimensional spatial geodetic observations, either by detecting early-warning signals of the tipping point of an earthquake based on the critical slowing down (CSD) effect of a state transition condition (19, 20) or by predicting/extending the time series of geodynamics for future seismic events based on dynamical models or the delay-embedding theorem (21, 22). Actually, to detect the early-warning signals of tipping points, the CSD concept has been widely applied in climate/ecosystem research and biomedical systems (19, 20). Moreover, to predict/

extend nonlinear time series by exploring high-dimensional spatial data, the spatiotemporal information (STI) transformation equations were theoretically derived based on the delay-embedding theorem (22) and were validated by data acquired from various real-world systems.

In this study, on the basis of the STI strategy with autoreervoir computing (23), we proposed a model-free method named real-time spatiotemporal information transformation learning (RSIT) in order to alert for possible catastrophic seismic events. RSIT combines nonlinear time-series prediction with tipping point detection, and has a solid theoretical background in both the delay-embedding theorem and state transition theory; thus, based only on high-dimensional time-series observations, this method can provide early-warning signals for upcoming state transitions by exploiting two critical phenomena or criteria of a nonlinear dynamical system approaching a tipping point, i.e., (a) the unpredictability/inconsistency (Fig. 1*B*) and (b) the instability/fluctuations (Fig. 1*C*). Specifically, by fully exploring spatial geodetic data based on the STI strategy, we can transform high-dimensional spatial observations into one-dimensional temporal time series of either (A) a target/explicit variable or (B) a latent/implicit variable. By unfolding the associated dynamics of the high-dimensional spatial variables, such a transformation extends the time series, thereby allowing the dynamic changes of either (A) the target variable representing the earthquake of the target location or (B) the latent variable representing the dynamics of the reduced geological system (one-dimensional center manifold near the tipping point) to be naturally predicted. Then, if the extension/prediction of the transformed time series for (A), i.e., (a) the unpredictability/inconsistency criterion of the STI strategy, becomes suddenly inaccurate at some time point, it can be considered an early-warning signal of an upcoming state transition or an earthquake due to the appearance of strongly nonlinear/nonstationary geodynamics near the change point or tipping point. Alternatively, if the transformed time series for (B), i.e., (b) the instability/fluctuation CSD criterion, starts to fluctuate strongly during this period, it implies that an earthquake is imminent due to the increased sensitivity to noise near the critical state or tipping point. In this way, the proposed RSIT method can be directly applied to high-dimensional real-time GNSS data or seismic waveform data (Fig. 1*D*).

From a data-driven analytics perspective, RSIT can efficiently transform raw high-dimensional spatial data into one-dimensional temporal data, naturally producing either the time-series extension/prediction of one target variable or the transformed time series of one latent variable on the basis of the STI equations combined with autoreervoir computing (Fig. 1*A–C*). Through this data reconstruction procedure, a series of future GNSS values for each target variable and the latent variable can be forecasted in a multistep-ahead way, and two criteria/indices can be estimated based on the STI equations and CSD theory: (a) the unpredictability detection index for measuring the difference or inconsistency between the predicted/extended and real values of (A) a target variable (Fig. 1*B*) and (b) the fluctuation detection index for quantifying the fluctuations of (B) the one-dimensional latent variable (Fig. 1*C*). Simultaneous changes in these two RSIT indices serve to identify an early-warning signal of a tipping point just before an imminent earthquake in a geodynamic system.

RSIT has significant advantages in three aspects: i) It can detect early-warning signals of high-magnitude earthquakes with higher accuracy than the existing methods by combining time-series prediction with critical state detection; ii) it requires much less computational time and fewer computational resources than traditional

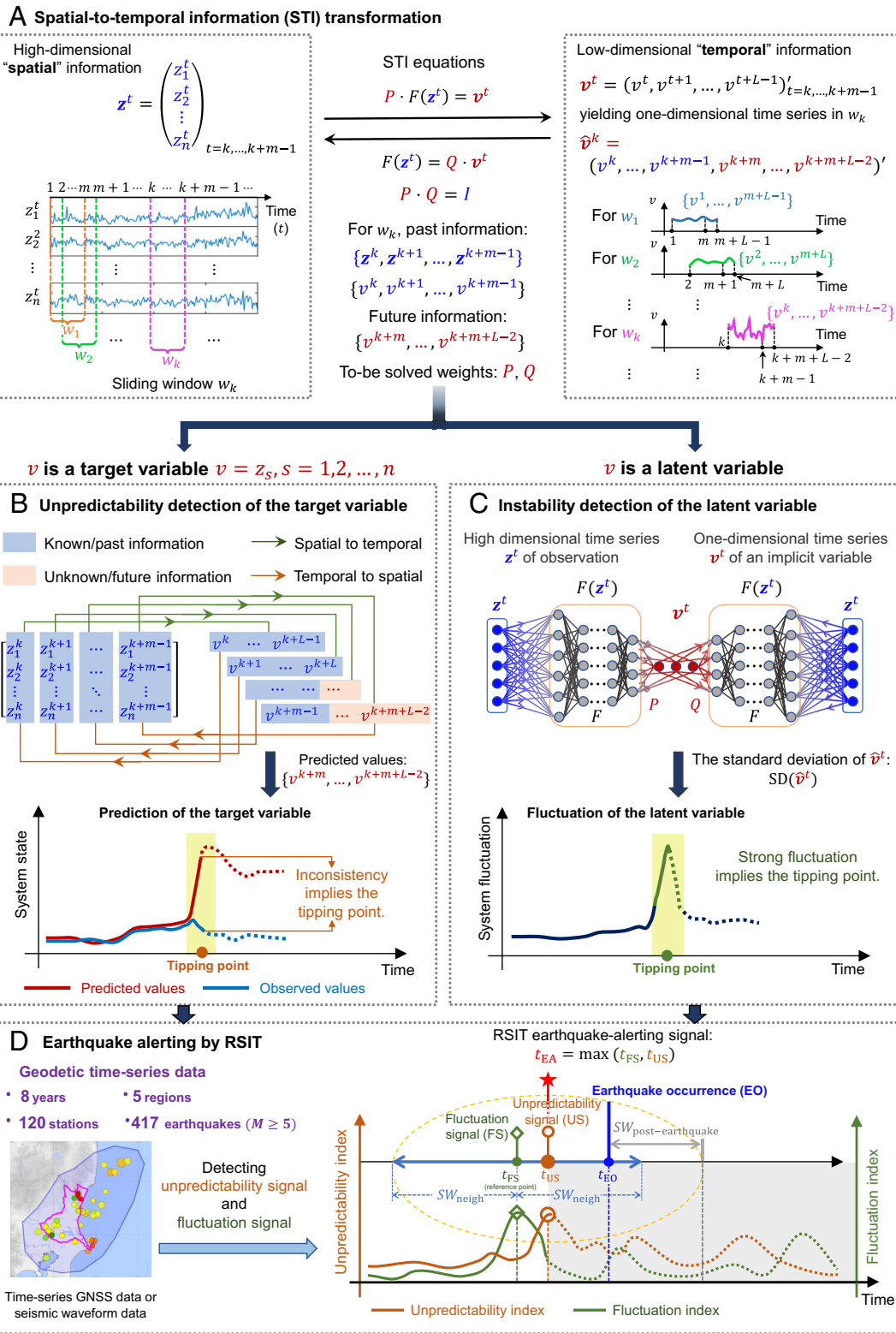


**Fig. 1.** Schematic illustration of RSIT. (A) The given high-dimensional "spatial" information  $\mathbf{z}^t$  and one-dimensional "temporal" information  $\mathbf{v}^t$  formed by the delay-embedding theorem can be transformed into each other based on the STI equations, where  $F$  represents an autoreservoir neural network whose weights are randomly given and fixed. Matrices  $P$  and  $Q$  are weight matrices to be determined by solving the STI equations. According to the information flow, RSIT has an autoencoder-like framework, that is,  $F(\mathbf{z}^t) \rightarrow \mathbf{v}^t \rightarrow F(\mathbf{v}^t) \rightarrow \mathbf{z}^t$ , different from but similar to the autoencoder structure  $\mathbf{z}^t \rightarrow \mathbf{v}^t \rightarrow \mathbf{z}^t$ . There are two ways to transform high-dimensional spatial information into one-dimensional temporal dynamics corresponding to two critical signals. (B)  $v$  is set as  $v = z_s$  ( $s = 1, 2, \dots, n$ ); that is,  $v$  is an explicit target variable selected from the high-dimensional variables as the target location or factor of the earthquake. Then, on the basis of the STI equations, the known/past spatial data are transformed into the unknown/future temporal information of the target variable  $z_s$ . Any significant inconsistency between the predicted transformed values and observed values of  $z_s$  implies unpredictability and thus implies the appearance of an early-warning signal of a tipping point/earthquake. (C)  $v$  is set as the latent variable, whose values are also transformed from the same known data by the STI equations. Here,  $v$  is the reduced one-dimensional system approximating the dominant dynamics or the center manifold of the geodynamical system near the tipping point. A drastic increase in the fluctuation of  $v$  signals an imminent critical transition/earthquake. (D) RSIT detects both the unpredictability signal (US) at  $t_{US}$  and the fluctuation signal (FS) at  $t_{FS}$  from GNSS time-series observations or seismic waveform data by the STI strategy with autoreservoir computing, which has the potential to provide early-warning signals of upcoming earthquakes from the above two signals.

neural network methods due to the nature of autoreervoir computing, in which all weights are randomly given in advance without training; and iii) it can be applied to real-time earthquake alert for a given region once the parameters are established. In applications involving GNSS or seismic waveform time-series data from various regions, namely, Sichuan Province of China, west-central Hokkaido of Japan, Ibaraki Prefecture of Japan, Miyagi Prefecture of Japan, and south-central Alaska of the United States, RSIT successfully alerted for most of strong earthquakes ( $M \geq 5$ ) and achieved 98.41% accuracy, 82.97% true-positive rate (TPR), and 0.98% false-positive rate (FPR) during recent years. These applications in different regions demonstrate the possible effectiveness and robustness of RSIT, which also suggests its potential for practical applications in the real-time early warning of earthquakes with high magnitudes. Based on the RSIT method, we also developed a web tool (publicly accessible at [https://earthquakepredictionrsit.com/eq\\_perdict](https://earthquakepredictionrsit.com/eq_perdict)) to find the abnormal local deformation precursors based on high-dimensional data, thus facilitating the detection of any potential early-warning signals of strong earthquakes in several regions.

## Results

With a sliding time window scheme, RSIT was applied to high-dimensional time series from both a numerical simulation (*SI Appendix, Fig. S1 and Note S1*) and GNSS observations or seismic waveforms in five high-risk earthquake zones/regions, namely, Sichuan Province of China, Ibaraki Prefecture of Japan, west-central Hokkaido (around Iburi) of Japan, Miyagi Prefecture of Japan, and south-central Alaska of the United States (Table 1). The input data for this study consisted of preprocessed GNSS and waveform time series. Missing values were filled using either cubic spline interpolation or a moving median strategy. Dense GNSS and waveform data were smoothed using average aggregation with a granularity of 24 h or 5 min, respectively (see *SI Appendix, Note S2* for details). The setting of sliding windows for the observed time series and the specific parameter setting for each region are described in *SI Appendix, Note S3 and Table S1*. The details of each region are provided in *SI Appendix, Note S4*. The metrics employed to evaluate the earthquake warning performance are described in *SI Appendix, Note S5*. According to the results, RSIT alerted for upcoming earthquakes with 93.21% accuracy and 99.00% specificity on average for 1,380 earthquakes with

$3 \leq M < 5$ , and 98.41% accuracy and 99.02% specificity on average for 417 strong earthquakes with  $M \geq 5$ . In addition, RSIT identified early-warning signals 6.27 d on average prior to the earthquakes with  $M \geq 5$  based on the daily GNSS data and 5.75 h on average prior to the earthquakes based on 5-min-long seismic waveform records. The alerting results of RSIT for the full time period of testing in each region are provided in *SI Appendix, Figs. S2–S6*. More computational details are provided in *SI Appendix, Tables S1–S5*. Besides, compared with the 10 existing methods M1–M10 (*Materials and Methods*), RSIT achieved the best accuracy and specificity in all regions, and produced far lower FPR (Table 2 and *SI Appendix, Tables S6–S10*).

**Earthquake Alerting in Japan.** Next, RSIT was used to alert for earthquakes in Japan. As a result of the active subduction and convergence among four lithospheric plates (the Pacific plate, North American plate, Eurasian plate and Philippine Sea plate) in the vicinity of the islands of Japan, almost one-tenth of the earthquakes on Earth occur in or around this region (24). Among these events, the crustal intraplate earthquakes have generally shallow focal depths with epicenters near the densely populated areas of Japan and therefore could lead to catastrophic casualties and damage. RSIT was applied to the high-dimensional GNSS time-series observations from several regions in Japan (Fig. 2), i.e., Ibaraki, west-central Hokkaido (around Iburi), and Miyagi. There are approximately 1,300 GNSS-receiver stations in Japan, from which we collected high-dimensional (1300D) GNSS time series of the daily elevation displacement (the change in elevation). In Japan, earthquake impact is also assessed by the Japan Meteorological Agency (JMA) seismic intensity scale, which describes the severity of shaking in specific locations during an earthquake, ranging from intensity 0 to intensity 7 (25). In this study, JMA intensity ( $I_{JMA}$ ) = 2, being felt by people keeping quiet in buildings (25), is set as the intensity cutoff to alert for earthquakes in Japan.

**Earthquake Alerting in Ibaraki Prefecture, Japan.** Ibaraki Prefecture in Japan lies in an area of complex tectonics near the intersection of four tectonic plates: the Pacific plate, the Okhotsk plate (a fragment of the North American plate), the Amur plate, and the Philippine Sea plate (26). Brisk seismic activities successively occur once every few years in southwest Ibaraki Prefecture, where the hypocenters of events tend to occur at a greater depth of approximately 50 km, and earthquakes tend to be of magnitude

**Table 1. Performance statistics of RSIT in various regions**

Indices Region	Monitoring years	Number of sliding windows*	Earthquake magnitude ( $M$ )	Number of earthquakes	TPR	FPR	Specificity	Accuracy	Average days ahead
All regions		10,962	$M \geq 5.0$	417	0.83	0.0098	0.9902	0.9841	6.27
			$3.0 \leq M < 5.0$	1,380	0.53	0.0100	0.9900	0.9321	6.08
Ibaraki	7	2,557	$M \geq 5.0$	133	0.82	0.0107	0.9893	0.9804	6.26
			$3.0 \leq M < 5.0$	387	0.64	0.0065	0.9935	0.9402	6.13
West-central Hokkaido	6	2,192	$M \geq 5.0$	52	0.81	0.0126	0.9874	0.9831	6.69
			$3.0 \leq M < 5.0$	100	0.45	0.0201	0.9799	0.9557	6.16
Miyagi	4	1,465	$M \geq 5.0$	157	0.85	0.0084	0.9916	0.9761	6.02
			$3.0 \leq M < 5.0$	200	0.60	0.0126	0.9874	0.9338	5.02
Sichuan	5	1,826	$M \geq 5.0$	14	0.93	0.0039	0.9961	0.9956	7.31
			$3.0 \leq M < 5.0$	322	0.34	0.0033	0.9967	0.8817	6.56
South-central Alaska	8	2,922	$M \geq 5.0$	61	0.80	0.0112	0.9888	0.9849	6.33
			$3.0 \leq M < 5.0$	371	0.56	0.0074	0.9926	0.9381	6.35

\*The setting of sliding-window scheme of the observed time series is presented in *SI Appendix, Note S3*.

**Table 2. Comparison of the earthquake-alerting performance of RSIT in five regions with that of the ten other existing methods**

Methods Region	Metrics	RSIT	M1	M2	M3	M4	M5	M6	M7	M8	M9	M10
Ibaraki	TPR	<b>0.82</b>	0.49	0.62	0.16	0.58	0.74	0.45	0.55	0.69	0.27	0.68
	Aggregative score	<b>0.87</b>	0.62	0.69	0.49	0.65	0.71	0.62	0.61	0.72	0.58	0.70
West-central Hokkaido	TPR	<b>0.81</b>	0.56	0.63	0.40	0.44	0.54	0.39	0.67	0.68	0.33	0.58
	Aggregative score	<b>0.80</b>	0.61	0.65	0.53	0.56	0.60	0.51	0.62	0.68	0.58	0.63
Miyagi	TPR	<b>0.85</b>	0.72	0.62	0.55	0.48	0.66	0.68	0.74	0.64	0.64	0.63
	Aggregative score	<b>0.92</b>	0.81	0.77	0.65	0.65	0.78	0.78	0.83	0.77	0.73	0.75
Sichuan	TPR	<b>0.93</b>	0.21	0.29	0.36	0.50	0.36	0.50	0.57	0.64	0.21	0.57
	Aggregative score	<b>0.86</b>	0.43	0.49	0.45	0.52	0.50	0.56	0.55	0.59	0.43	0.55
South-central Alaska	TPR	<b>0.80</b>	0.54	0.59	0.49	0.31	0.51	0.62	0.59	0.61	0.43	0.59
	Aggregative score	<b>0.80</b>	0.58	0.63	0.52	0.46	0.59	0.63	0.61	0.65	0.63	0.59

\*Aggregative score is the average of TPR, precision and accuracy. The performance on other statistic indices can be seen in *SI Appendix, Tables S6–S10*. The largest values were marked by bold typeface.

M5.0–M6.0 (27). Twenty-two GNSS stations are distributed across Ibaraki (Fig. 2*A*). The epicenters of a series of earthquakes that occurred around Ibaraki Prefecture are shown in Fig. 2*B*. RSIT was applied to the 22-dimensional time series (Fig. 2*C*), with the parameter setting shown in *SI Appendix, Table S1*. Among all 133 strong earthquakes with  $M \geq 5$  and  $I_{JMA} \geq 2$  that occurred in Ibaraki during a period of 7 y from January 1, 2015 to January 1, 2022, RSIT successfully alerted for most of them with 6.26 d ahead on average, achieving 98.04% accuracy, 98.93% specificity, 0.82 TPR and only 0.0107 FPR (Table 1).

**Earthquake Alerting in West-Central Hokkaido, Japan.** The island of Hokkaido is located to the north of the main island of Honshu and exhibits mountainous and volcanic plateau landforms. It is one of the most tectonically active regions in Japan and is influenced by both the westward subduction of the Pacific plate and the convergence between the North American and Eurasian plates (28). Hence, like many areas of Japan, Hokkaido is seismically active. Since 1980, the island has been struck by a series of massive ( $M \geq 6$ ) earthquakes, such as the earthquakes that occurred in 1993, 2003 and 2018 (with magnitudes of M7.6, M8.3, and M6.6, respectively). There are 35 GNSS stations in west-central Hokkaido (around Iburi), and their distribution is shown in Fig. 2*D*.

During a period of 6 y from January 1, 2016 to January 1, 2022, 52 strong earthquakes with  $M \geq 5$  and  $I_{JMA} \geq 2$  occurred across west-central Hokkaido. Based on the 35-dimensional GNSS time-series observations obtained during these years, RSIT yielded early-warning signals for these earthquakes with 6.69 d ahead on average, achieving 98.31% earthquake-warning accuracy, 98.74% specificity, 0.81 TPR and 0.0126 FPR (Table 1). The graphic display of how RSIT works is shown in Fig. 2*F* and *G*. More performance details are provided in Table 1 and *SI Appendix, Table S2*.

**Earthquake Alerting in Miyagi Prefecture.** Miyagi Prefecture is located in the Tohoku region of Honshu which lies at the intersection among three tectonic plates: the Eurasian, Philippine, and North American plates (29). Severe earthquakes strike this region almost cyclically (approximately every 40 y); examples include large earthquakes that occurred in 1793, 1835, 1861, 1897, 1936, and 1978. There are 23 GNSS stations in Miyagi,

and their geographical distributions are presented in Fig. 2*E*. RSIT was applied to the 23-dimensional GNSS time-series observations from this region (Fig. 2*H* and *I*).

For the early warning of the strong earthquakes ( $M \geq 5$ ) that struck the Miyagi region from January 1, 2008 to January 1, 2012, RSIT achieved 97.61% accuracy and 99.16% specificity and provided early-warning signals 6.02 d prior to the earthquakes on average (Table 1). In addition, RSIT alerted for most 200 ( $3 \leq M < 5$ ) earthquakes effectively, reaching 93.38% accuracy and 98.74% specificity. More details of the earthquake-alerting performance are provided in Table 1 and *SI Appendix, Table S2*.

**Earthquake Alerting in Sichuan, China.** Sichuan is a landlocked province occupying most of the so-called Sichuan Basin in Southwest China, which is located within the Eurasian plate near its boundary with the Indian plate. The Sichuan Basin has historically shown low levels of seismic activity, but over the past few decades, especially since 2015, earthquake activity therein has experienced an unprecedented trend of continuous growth, and the magnitude of events has been increasing; for example, the magnitude 5.7 Xingwen earthquake and the magnitude 6.0 Changning earthquake occurred in 2018 and 2019, respectively (30). There are two types of time-series data in the Sichuan Basin, i.e., 1) daily records of vertical displacements derived from 24 GNSS stations (distributed as shown in Fig. 3*A*) and 2) 5-min-long seismic waveform records (31) derived from 37 seismic stations (distributed as shown in Fig. 3*B*).

From January 1, 2017 to January 1, 2022, fourteen strong earthquakes with  $M \geq 5$  occurred in Sichuan, the majority of which were alerted by RSIT 7.31 d prior to the event, reaching 99.56% accuracy, 99.61% specificity, 0.93 TPR and 0.0039 FPR (Table 1). In Fig. 3, we illustrate how RSIT alerts for several major earthquakes in Jiuzhaigou and Changning. Based on the daily GNSS time series, the early-warning signal provided by RSIT is 4/2 d prior to the earthquake that occurred in Jiuzhaigou/Changning (Fig. 3*C* and *D* and *SI Appendix, Table S2*). Based on the 5-min-long waveform records, the early-warning signal provided by RSIT is 2.92/8.58 h prior to the earthquake that occurred in Jiuzhaigou/Changning (Fig. 3*E* and *F* and *SI Appendix, Table S3*). More details of the earthquake-alerting performance are provided in Table 1 and *SI Appendix, Tables S2–S3*.

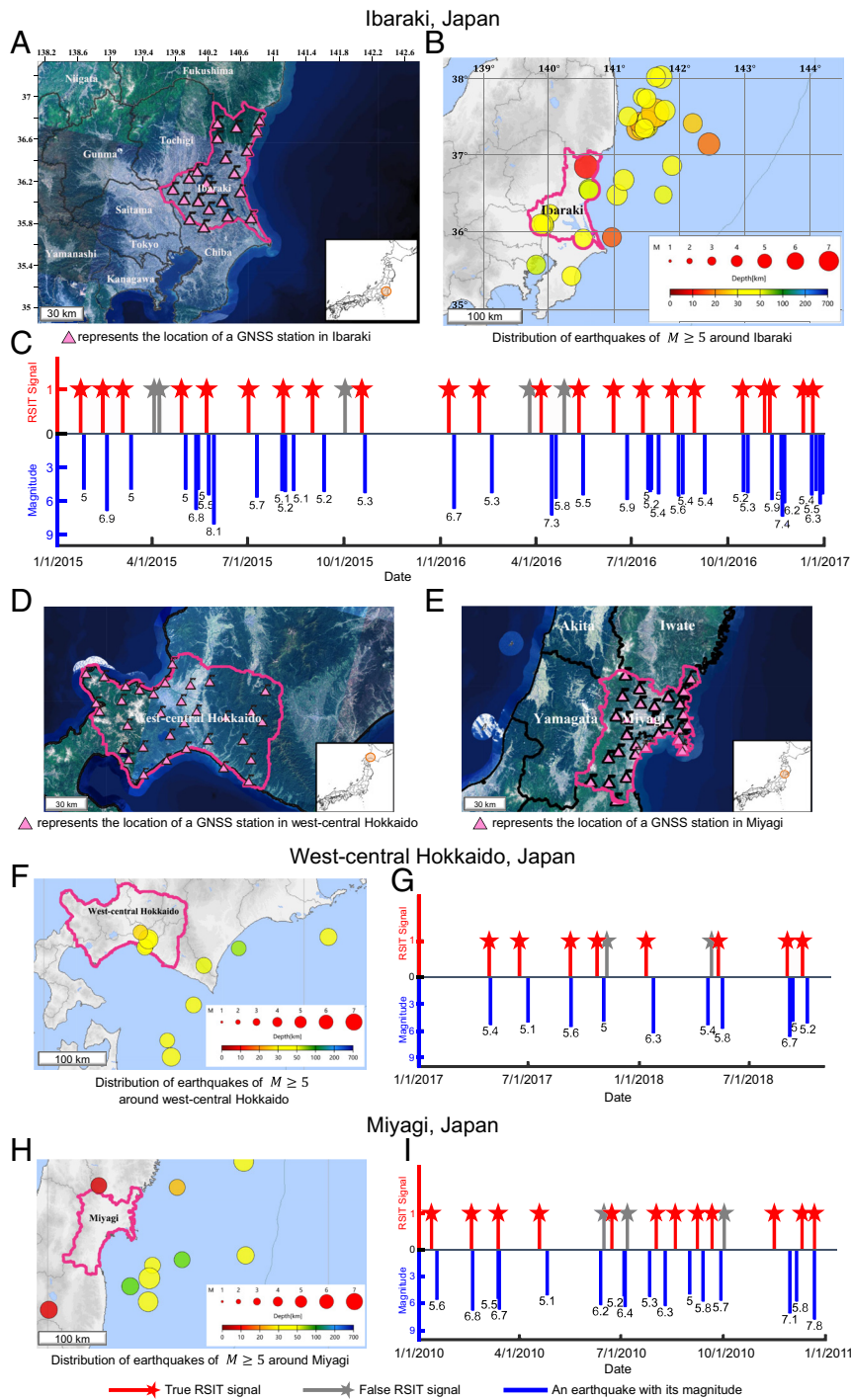


**Fig. 2.** Possible early-warning signals of earthquakes with  $M \geq 5.0$  provided by RSIT based on the high-dimensional GNSS time series from three regions in Japan. (A) The geographic distribution of 22 GNSS stations in Ibaraki. (B) The geographic distribution of the epicenters of 38 earthquakes with  $M \geq 5.0$  around Ibaraki, from January 1, 2015 to January 1, 2017. (C) Alerted earthquakes around Ibaraki. Totally 35 earthquakes (blue bars) were signaled (red stars) in advance by RSIT, and only five false signals (gray stars) occurred during these 2 y. (D) The geographic distribution of 35 GNSS stations in west-central Hokkaido. (E) The geographic distribution of 35 earthquakes with  $M \geq 5.0$  around west-central Hokkaido, from January 1, 2017 to October 10, 2018. (F) The earthquake-alerting performance of RSIT around west-central Hokkaido. (G) The earthquake-alerting performance of RSIT around Miyagi. (A, D, E) Copyright Geospatial Information Authority of Japan. (B, F, H) Copyright Japan Meteorological Agency.

### Earthquake Alerting in South-Central Alaska, United States.

South-central Alaska, located at the northern junction between the North American plate and the Pacific plate along the Circum-Pacific Ring of Fire, is one of the most geologically active regions of the world (32). Based on the GNSS time-series observations (the sampling frequency of the data is 1/86,400 Hz, i.e., daily GNSS data) in south-central Alaska, RSIT was applied to detect the warning signals for earthquakes from January 1, 2014 to January 1, 2022. During the 8 y, there are 61 strong earthquakes with  $M \geq 5$  occurred in south-central Alaska. RSIT succeeded in alerting for the majority of earthquake events with an average of 6.33 d ahead, reaching 98.49% accuracy, 98.88% specificity, 0.80 TPR and 0.0112 FPR (Table 1). More details are provided in *SI Appendix, Table S2*.

As shown in Fig. 4, the two major earthquakes that struck south-central Alaska in November 2018 were alerted based on the GNSS data of the frequency of 1/300 Hz, i.e., one value every 5 min. The early-warning signals were provided by RSIT at 4:31 AM November 20, 2018 and 1:54 AM November 30, 2018, respectively, prior to the seismic events, and there were no FPs, achieving 100% accuracy and 100% specificity (*SI Appendix, Table S3*).

More applications of RSIT to earthquake datasets, including the GNSS time-series data from south-central Alaska in the United States (with different sampling intervals or frequencies from those stated in the main text), Fukushima Prefecture and Kumamoto Prefecture of Japan, are provided in *SI Appendix, Fig. S7*. Details of the applications are described in *SI Appendix, Notes S6–S8*.

# Sichuan, China

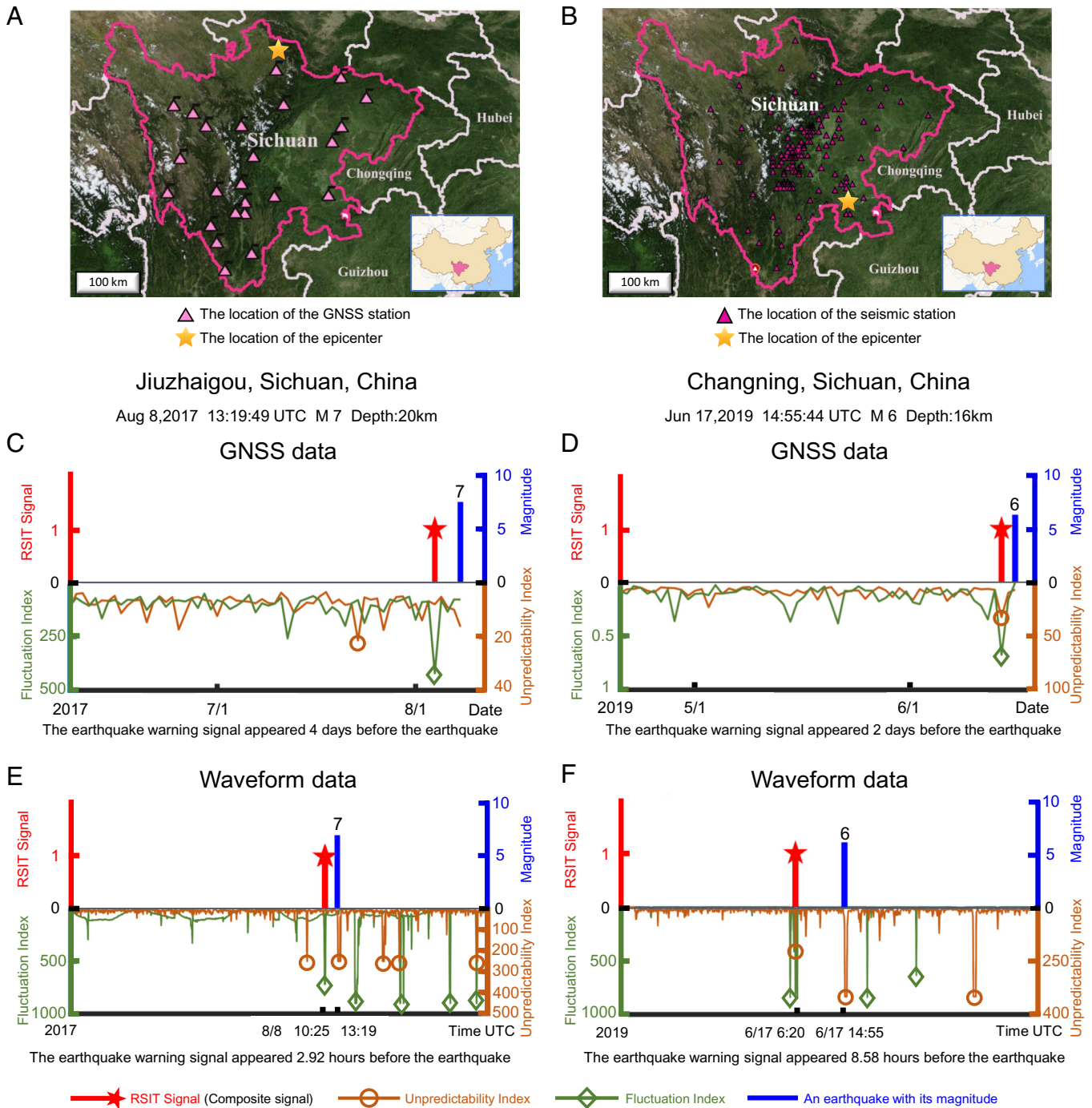


**Fig. 3.** Alerting for earthquakes by RSIT in Sichuan, China, based on high-dimensional real-time GNSS data and seismic waveform data. (A) The geographic distribution of the 24 GNSS stations in Sichuan. (B) The geographic distribution of the 37 seismic stations in Sichuan. (C) The RSIT signal for the M7.0 earthquake based on the GNSS time series in Jiuzhaigou, Sichuan, from June 8, 2017 to August 8, 2017. (D) The RSIT signal of the M6.0 earthquake based on the GNSS time series in Changning, Sichuan, from April 20, 2019 to June 17, 2019. (E) The RSIT signal for the M7.0 earthquake based on the waveform time series in Jiuzhaigou, Sichuan, from August 5, 2017 to August 9, 2017. (F) The RSIT signal for the M6.0 earthquake based on the waveform time series in Changning, Sichuan, from June 16, 2019 to June 18, 2019. (A, B) Copyright 2021 AutoNavi - GS(2019)6379.

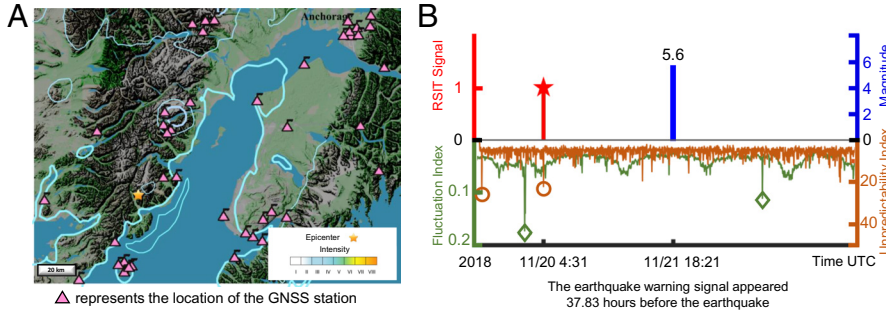
## Factors That Affect the Earthquake-Alerting Performance.

Seismic events are categorized into different types on the basis of the magnitudes of earthquakes based on United States Geological Survey (USGS): micro ~ light (M1.0–M4.9), and moderate ~ great (M5.0–above). Minor quakes with magnitude below M4.9 occur frequently worldwide, and generally cause little damage. Stronger quakes with magnitude larger than M5.0 may cause catastrophic damages. It is difficult to alert for all earthquakes, since most of

shocks are micro ~ light. Therefore, the proposed RSIT is designed to alert for moderate ~ great (M5.0–above) earthquakes. On the other hand, in some countries like Japan, the JMA intensity scale is also employed to describe the severity of damages from the event on a scale from  $I_{JMA} = 0$  to  $I_{JMA} = 7$ , with  $I_{JMA} = 0$  being imperceptible to people and  $I_{JMA} = 7$  being severe damage to many residences (25). Generally, high-intensity earthquakes (i.e., stations are near epicenters)

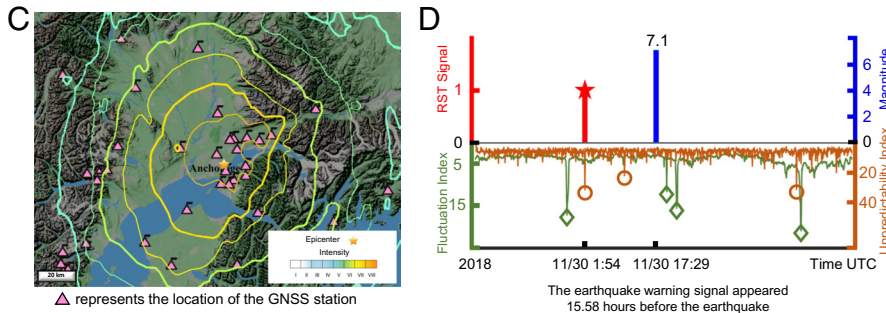
Pedro Bay, Alaska, USA

Nov 21, 2018 18:21:44 UTC M5.6 Depth:143.3km



Anchorage, Alaska, USA

Nov 30, 2018 17:29:29 UTC M7.1 Depth:46.7km



★ RSIT Signal (Composite signal)    ○ Unpredictability Index    ◇ Fluctuation Index    — An earthquake with its magnitude

**Fig. 4.** RSIT alerts for earthquakes based on the high-dimensional GNSS time series in south-central Alaska in the United States. (A) The geographic distribution of GNSS stations and intensities of the magnitude M5.6 earthquake that occurred in Pedro Bay, Alaska. (B) The RSIT performance from November 19 to 23, 2018. (C) The geographic distribution of GNSS stations and intensities of magnitude M7.1 earthquake that occurred in Anchorage, Alaska. (D) The RSIT performance from November 27 to December 1, 2018. (A, C) Copyright 2021 GS(2011)6020 Google and USGS.

are with shallow focal depths, or with large magnitudes, or with both features (33, 34). Thus, intensity is an effective scale for measuring the destruction of earthquakes. In this study,  $I_{JMA} = 2$ , which is felt by people keeping quiet in buildings (25), is set as the intensity cutoff to alert for earthquakes in Japan so that any earthquake that has a nonnegligible impact on the studied region can be considered (SI Appendix, Fig. S8). In a word, in order to alert for destructive earthquakes as accurately as possible and minimize false-positive signals, the proposed RSIT is designed to detect early-warning signals for possible earthquakes with high magnitudes (M5.0–above) and high intensities (Intensity 2–above).

As presented in Tables 1 and 3, it is seen that the RSIT can alert for most moderate ~ great earthquakes with much better performance. Furthermore, we have also showed the detailed performance of RSIT on alerting for earthquakes with magnitudes  $M \geq k$ ,  $k = 3, 4, 5, 6$  for each region as presented in SI Appendix, Table S5 and Note S9, from which it is seen that  $M \geq 5$  is the best magnitude cutoff for applying RSIT.

Focal depth is another factor that affects the destruction level of an earthquake. Most earthquakes occur at depths less than 70 km, and generally, shallower earthquakes are more destructive (35). To better analyze the earthquake-alerting performance, we evaluated the performance on three groups of earthquake events, i.e., i) very shallow earthquakes with focal depths less than or equal to 30 km, ii) other shallow earthquakes with focal depths between 30 km and 70 km, and iii) deeper earthquakes with focal depths more than or equal to 70 km. Generally, RSIT works better in alerting for earthquakes with shallow focal depths. However, it still detects the early-warning signals for most high-magnitude earthquakes even with deep focal depths (Table 3). Overall, compared with the magnitude, the impact of the earthquake depth is relatively small for RSIT.

The epicenter positions of earthquake events in some coastal regions were divided into two categories, i.e., “on-land” and “off-shore” earthquakes. As shown in Table 3 and SI Appendix, Fig. S9 and Table S4, RSIT generally works better in alerting for on-land

strong earthquakes. Moreover, as a type of earthquake precursors, the surface deformation can be found far away from the epicenter, that is, there could be distant surface deformation preceding a high-magnitude earthquake, according to the various empirical formulas estimating the radius of the effective precursor manifestation zone (36). Therefore, the abnormal change/signal of the surface deformation captured by a few GNSS monitoring stations may be related to an imminent strong earthquake several hundred kilometers away. In theory, the proposed method may alert for a long-range earthquake with high magnitude by detecting abnormal surface deformation based on real-time observation from many GNSS monitoring stations. However, the practical application shows the limitation that RSIT generally performs better in alerting for earthquakes at close ranges than for those at long ranges (SI Appendix, Note S9 and SI Appendix, Fig. S8 and Table S11).

In summary, the above computations show that 1) RSIT is effective and accurate in alerting for those earthquakes with magnitude  $M \geq 5$ ; 2) RSIT can provide valid early-warning signals for  $M \geq 5$  earthquakes with shallow or deep focus. 3) Generally, RSIT works better in alerting for on-land earthquakes ( $M \geq 5$ ). 4) In general, RSIT demonstrates better performance to alert for earthquakes with epicenters in proximity to GNSS stations.

## Discussion

Earthquakes have been taking countless human lives and destroying vast swathes of property. Accordingly, methods for accurately and robustly detecting earthquake precursors and generating early-warning signals are urgently needed, although such a target is notoriously difficult and challenging. The rapid development of geodetic technology, however, has created an opportunity to observe the Earth’s surface simultaneously in real-time with GNSS platforms from a number of positions. On the basis of this technology, we developed RSIT to detect the local deformation precursors, which may serve as the prelude of strong earthquakes. We realize that in

**Table 3. Earthquake-alerting performance of RSIT in each region**

Region	Classification of events Magnitude	TPR					FPR				
		On land	Offshore	Depth ≤ 30 km	30 < Depth ≤ 70 km	Depth > 70 km	On land	Offshore	Depth ≤ 30 km	30 < Depth ≤ 70 km	Depth > 70 km
Ibaraki (January 1, 2015– January 1, 2022)	$M \geq 5.0$	0.91	0.79	0.87	0.80	0.88	0.0103	0.0106	0.0103	0.0106	0.0102
	$3.0 \leq M < 5.0$	0.62	0.66	0.69	0.61	0.69	0.0059	0.0059	0.0057	0.0061	0.0055
West-central Hokkaido (January 1, 2016– January 1, 2022)	$M \geq 5.0$	0.77	0.82	1.00	0.77	0.73	0.0124	0.0125	0.0124	0.0125	0.0124
	$3.0 \leq M < 5.0$	0.51	0.34	0.55	0.45	0.31	0.0197	0.0195	0.0193	0.0197	0.0193
Miyagi (January 1, 2008– January 1, 2012)	$M \geq 5.0$	0.92	0.83	0.81	0.90	0.69	0.0076	0.0083	0.0078	0.0080	0.0076
	$3.0 \leq M < 5.0$	0.60	0.60	0.53	0.61	0.75	0.0115	0.0120	0.0115	0.0118	0.0111
South-central Alaska (January 1, 2014– January 1, 2022)	$M \geq 5.0$	0.81	0.79	0.86	0.68	0.86	0.0111	0.0111	0.0110	0.0110	0.0110
	$3.0 \leq M < 5.0$	0.52	0.60	0.59	0.58	0.50	0.0069	0.0070	0.0069	0.0067	0.0067
Sichuan (January 1, 2017–January 1, 2022)	$M \geq 5.0$	0.93	NaN*	0.93	NaN*	NaN*	0.0039	NaN*	0.0039	0.0038	0.0038
	$3.0 \leq M < 5.0$	0.34	NaN*	0.34	NaN*	NaN*	0.0033	NaN*	0.0033	0.0027	0.0027

\*NaN means there is no such event.

addition to earthquakes, there are many other causes of local surface deformation (37, 38), such as landslides, engineering blasting, and volcanic eruptions (39), which may bring false-positive signals in earthquake alert (SI Appendix, Note S10). But this is still a valuable reference for the seismic geohazard monitoring and warning.

Generally, due to the high nonlinearity and nonstationarity of geodynamic phenomena, it is difficult to detect the tipping points or state transition points in many real-world systems, especially geodynamical systems (40), based on GNSS observations. By focusing on two key features, i.e., the unpredictability and instability of the high-dimensional time-series data near the tipping point of a nonlinear dynamical system, we developed the RSIT strategy based on the STI equations, which could robustly and accurately provide early-warning signals of the critical change in high-dimensional GNSS and seismic waveform values. Specifically, RSIT first transforms high-dimensional spatial information into one-dimensional temporal dynamics for each target variable and a single latent variable based on the STI equations. Then, the two extended one-dimensional time series are used for nonlinear time-series prediction (the unpredictability criterion with the delay-embedding theorem) and tipping point detection (the instability criterion with the CSD theorem), which are conducted simultaneously to robustly detect precursors and early-warning signals of earthquakes. Considering that the pre-seismic movement in imminent earthquakes is one of the main causes of abnormal and significant changes in geodetic values, an upcoming earthquake may thus be robustly alerted. Furthermore, from a dynamical systems viewpoint, short-term geodetic time-series data recorded in the recent past should contain much more information on the near-future evolution of a geodynamical/seismic system than time-series data recorded in the distant past owing to the time-varying, nonstationary nature of natural phenomena. RSIT can transform recently recorded short-term high-dimensional data into future time series by exploiting high-dimensional spatial information to compensate for short-term data, thus making robust earthquake warnings.

On the basis of high-dimensional GNSS time-series observations and seismic waveform data from a number of regions across recent 4 to 8 y, RSIT detected the early-warning signals of strong earthquakes with high accuracy and low FPRs, and performed better than ten existing methods, thereby demonstrating the effectiveness of the proposed method. In addition, compared with traditional deep learning methods, RSIT relies on an autoregressive neural network, which does not require the training of a massive number of parameters and thus takes much less computational time and

resources; hence, RSIT is suitable as a complementary and synergistic method of the widely used short-term seismicity-based models, such as the Epidemic Type Aftershock Sequence (ETAS) model (41, 42) and the STEP model (43), which can forecast earthquakes in a statistical way based on the information of historical earthquakes. We will further explore the possibility of improving the RSIT method based on the seismic catalogs and ensemble modeling technique of the Collaboratory for the Study of Earthquake Predictability (CSEP) (44) in two aspects. First, for each specific earthquake prone area, instead of using the empirical parameters, it may be promising to train the parameters of RSIT for elaborate event classifications such as different geological conditions, earthquake magnitudes, epicenter locations, and other classifications according to historic seismic catalogs. Second, we will develop an ensemble method which employs both the GNSS-based RSIT method and the seismicity-based forecasting models as simultaneous weak learners, and make a decision of the final earthquake alert by combining their signals, e.g., by voting.

The real-data applications presented herein show that RSIT performs better at detecting the possible early-warning signals of moderate ~ great earthquakes with magnitudes  $M5.0$  or above and with terrestrial epicenters or shallow focal depths (Table 3), which implies that those strong earthquakes may occur with different geodynamical mechanisms from other earthquakes (1, 40). Although it has been shown that the alerting accuracy of RSIT outperforms those of previous methods, it is an important future task to further improve RSIT toward practical use. Clearly, how to accurately detect early-warning signals of low-magnitude (or low-intensity) earthquakes and events with deep focal depths or epicenters under the sea is still challenging for RSIT and should be further studied and solved in the future.

## Materials and Methods

**Spatiotemporal Information (STI) Transformation.** High-dimensional spatial variables of geodetic observations from a geodynamical system contain abundant information on its future evolution, which can be exploited for the robust analysis and warning of seismicity. The STI strategy, which is theoretically based on the delay-embedding theorem (21, 44), is derived to transform the spatial information of multi-variables into the temporal dynamics of a target variable. We use the following notations:  $\mathbf{z}^t = (z_1^t, z_2^t, \dots, z_n^t)$  is an  $n$ -dimensional vector of observed values from  $n$  geodetic observation stations at time point  $t$ , where the symbol “ $t$ ” represents a transpose, and  $(\mathbf{z}^1, \mathbf{z}^2, \dots, \mathbf{z}^m)$  is a matrix of the observed high-dimensional time series with  $m$  time points in a sliding time window  $w_1$  (Fig. 1A). The calculation in other time windows is similar.

First, from the delay-embedding theorem, we define an  $L$ -step delay-embedding transform of a scalar variable  $v$ , such that for a time series (vector)  $\mathbf{v}^t = (v^t, v^{t+1}, \dots, v^{t+L-1})'$  with  $m$  time points,

$$(\mathbf{v}^1, \mathbf{v}^2, \dots, \mathbf{v}^m) = \begin{pmatrix} v^1 & v^2 & \dots & v^m \\ v^2 & v^3 & \dots & v^{m+1} \\ \vdots & \vdots & \ddots & \vdots \\ v^L & v^{L+1} & \dots & v^{m+L-1} \end{pmatrix}_{L \times m}, \quad [1]$$

Here, the parameter  $L > 1$  is also known as the embedding dimension. Then, for a set of high-dimensional time-series observations

$$(z^1, z^2, \dots, z^m) = \begin{pmatrix} z_1^1 & z_2^1 & \dots & z_n^1 \\ z_1^2 & z_2^2 & \dots & z_n^2 \\ \vdots & \vdots & \ddots & \vdots \\ z_1^m & z_2^m & \dots & z_n^m \end{pmatrix}_{n \times m}, \quad [2]$$

with  $n$  variables and  $m$  time points, there are the following STI equations (22, 23):

$$\begin{cases} \Phi(z^t) = \mathbf{v}^t, \\ z^t = \Psi(\mathbf{v}^t), \end{cases} \quad [3]$$

where  $\Phi: \mathbb{R}^n \rightarrow \mathbb{R}^L$  and  $\Psi: \mathbb{R}^L \rightarrow \mathbb{R}^n$  are nonlinear differentiable functions satisfying  $\Phi \circ \Psi = id$ , the symbol " $\circ$ " is the function composition operation, and  $id$  represents the identity function. In Eq. 3, the first equation is the primary STI equation, and the second is its conjugate form. Actually, Eq. 1 is a Hankel matrix that is constructed by a one-dimensional time series of  $v$ . According to Takens' embedding theorem and its generalized versions, a delay-embedding scheme  $\mathbf{v}^t$  can be used to reconstruct the topologically equivalent dynamics of the original system  $z^t$  if  $L > 2d > 0$  under generic conditions (21), where  $d$  is the box-counting dimension of the original attractor and is usually small due to dissipation in real-world systems (44). The first equation of Eq. 3 clearly maps  $\mathbf{z}^t$  to  $\mathbf{v}^t$ , which actually transforms multivariable spatial information  $(z_1^t, z_2^t, \dots, z_n^t)$  at one time point/instant  $t$  into the univariable temporal information  $(v^t, v^{t+1}, \dots, v^{t+L-1})$  over multiple time points  $\{t, t+1, \dots, t+L-1\}$ . Therefore, the dynamics of the  $n$ -dimensional system can be represented by one-dimensional data with the delay-embedding theorem. The details of Takens' embedding theorem are provided in *SI Appendix, Note S11*.

Second, due to the high nonlinearity and time-varying nonstationarity of the underlying geodynamics (45), the most recent short-term time series usually contain more reliable information on the dynamics of the immediate future than the distant-past time series. Thus, the problems posed by nonstationarity and nonlinearity can be alleviated by using high-dimensional short-term data (i.e., in a sliding time window), provided that this high-dimensional spatial information can be transformed into one-dimensional temporal information to compensate for the short-term data by the STI equations. However, it is difficult to estimate the nonlinear maps  $\Phi$  and  $\Psi$  with only short-term time series. By taking a nonlinear function  $F$  as an autore reservoir structure based on both the primary and the conjugate forms of the STI equations, we approximate the STI equations of Eq. 3 into simpler forms:

$$\begin{cases} PF(z^t) = \mathbf{v}^t, \\ F(z^t) = Q\mathbf{v}^t, \end{cases} \quad [4]$$

where  $PQ = I$ ,  $P$  is an  $L \times \bar{n}$  matrix,  $Q$  is an  $\bar{n} \times L$  matrix,  $I$  represents an  $L \times L$  identity matrix, and  $F = (F_1, F_2, \dots, F_{\bar{n}})'$  is a nonlinear function (autore reservoir), with  $F_k: \mathbb{R}^n \rightarrow \mathbb{R}$ . The autore reservoir  $F$  is actually a multilayer neural network with interconnected nodes, among which the weights are randomly given and fixed in advance (rather than trained) in the computation (44, 46). Thus, Eq. 4 can be efficiently solved in contrast to the original Eq. 3. A detailed description

of the autore reservoir and STI equations [4] are provided in *SI Appendix, Note S11*. Based on the explicit target variable or the implicit latent variable  $v$ , there are two different forms of the STI equations:

1. Predicting an explicit/target variable:  $v$  is set as a target variable  $v = z_s^t (s = 1, 2, \dots, n)$ , and  $\mathbf{v}^t = (v^t, v^{t+1}, \dots, v^{t+L-1})' = (z_s^t, z_s^{t+1}, \dots, z_s^{t+L-1})' = \mathbf{z}_s^t$  is a vector of time series with  $t = 1, 2, \dots, m$ . Thus,  $(v^1, v^2, \dots, v^m)'$  are observable values of  $v$ , while  $(v^{m+1}, v^{m+2}, \dots, v^{m+L-1})'$  are future/unknown values. Then, by solving the STI equations of Eq. 4, we can obtain the  $L - 1$  future values  $(v^{m+1}, v^{m+2}, \dots, v^{m+L-1})' = (z_s^{m+1}, z_s^{m+2}, \dots, z_s^{m+L-1})'$  beyond the current time point  $m$ , which are transformed from the high-dimensional spatial information  $z^t, t = 1, 2, \dots, m$ . Far from the tipping point, since the geodynamical system is stable, the predicted/extended values are considered accurate and expected to be close to the observed values within each sliding time window of the time series. However, when the geodynamical system approaches the tipping point or transition point, the nonlinear terms dominate the geodynamics; consequently, the predicted/extended values become inconsistent with the observed values. In this situation, the so-called unpredictability/inconsistency signal can be identified by solving the target variable-based STI equations (TV-STI Eq. 4) when  $v$  is a target variable.

2. Predicting the implicit/latent variable:  $v$  is set as a latent variable, where both  $(v^1, v^2, \dots, v^m)'$  and  $(v^{m+1}, v^{m+2}, \dots, v^{m+L-1})'$  are unknown values of  $v$ . We can obtain these  $m + L - 1$  values by solving Eq. 4. The STI equations transform/reduce high-dimensional spatial information  $z^t$  to the dynamics of the latent variable  $v$ , which approximately represents the dominant dynamics of the original system. When the geodynamical system is in a stable equilibrium far from the tipping point, there is no CSD phenomenon occurring in such one-dimensional dynamics  $\{v^1, v^2, \dots, v^{m+L-1}\}$ . However, when the geodynamical system approaches the tipping point, strong fluctuations of the one-dimensional center manifold dynamics of  $\{v^1, v^2, \dots, v^{m+L-1}\}$  arise based on the CSD principle or dynamical network marker conditions (19) due to the increased sensitivity to noise. In other words, the so-called fluctuation/instability signal can be identified by solving the latent variable-based STI equations (LV-STI Eq. 4) when  $v$  is the latent variable.

Therefore, for a time point or certain period, RSIT can detect the significant change of geodetic values (e.g., GNSS and seismic waveform values) based on both of the above criteria, that is, by detecting the unpredictability signal from the TV-STI equations at the same time as the fluctuation signal from the LV-STI equations. The details of the two criteria are given in the following sections.

**Detecting the Unpredictability/Inconsistency Signal Based on STI Equations of Each Target  $\mathbf{v}^t$ .** The first early-warning signal from RSIT is the unpredictability or inconsistency signal, the appearance of which indicates that the geodynamical system has become "unpredictable" via the STI equations due to approaching a catastrophic transition or an earthquake.

As shown above, the criterion of the unpredictability signal detection is based on the TV-STI equations; that is, the value of each geodetic variable at the target station is chosen as one target variable for prediction. By setting  $v^t = z_s^t (s = 1, 2, \dots, n)$ , there are observed/known values  $\{v^1, v^2, \dots, v^m\} = \{z_s^1, z_s^2, \dots, z_s^m\}$  in the upper left part of the matrix in Eq. 1 and unknown values  $\{v^{m+1}, v^{m+2}, \dots, v^{m+L-1}\}$  in the lower right corner, where  $m$  is the number of time points (i.e., the size of the sliding time window), and  $L$  is the embedding dimension. These unknown values are the to-be-predicted future information of the target station. By solving the TV-STI equations (Eq. 4 with  $v^t = z_s^t$ ), we obtain the  $L - 1$  unknown values  $\{v^{m+1}, v^{m+2}, \dots, v^{m+L-1}\}$ , and the weight matrices  $P$  and  $Q$ . The details of solving the TV-STI equations are provided in *SI Appendix, Note S12*.

Specifically, for each target variable  $z_s (s = 1, 2, \dots, n)$  of station  $s$ , RSIT evaluates the loss or the RMSE between the predicted/extended values  $\{v^{m+1}, v^{m+2}, \dots, v^{m+L-1}\}$  and the true/observed values  $\{z_s^{m+1}, z_s^{m+2}, \dots, z_s^{m+L-1}\}$  with a sliding time window (*SI Appendix, Fig. S10*). The Student  $t$  test is applied to estimate the difference between the loss of station  $s$  at time point  $t$  and its previous errors (*SI Appendix, Notes S12 and S13*). Based on the  $P$ -value of significance, we decide whether there is a significant difference between the errors from current and from the previous time points for station  $s$ . If the average  $P$ -value is smaller than a significance level

threshold for all stations, we identify an unpredictability signal, and record the corresponding time point as  $t_{US}$ .

Generally, it is possible to accurately predict future dynamics by using the STI equations when the lithosphere system is in a stable state (47). However, future geodetic values (such as GNSS values) cannot be accurately predicted if the system approaches a tipping point/critical state. Theoretically, when a dynamical system is close to a critical state, the linear terms cannot approximate the dynamics; instead, the nonlinear terms dominate the geodynamics based on bifurcation theory (20, 48), leading to an increase in the difference between the ground truth and the predicted/extended values, which is employed as the inconsistency signal. The rise of this inconsistency signal, namely, a significant difference between the predicted/extended values and the observed values, indicates an imminent tipping point or critical state, and thus is the first type of an early-warning signal for a possible earthquake.

**Detecting the Fluctuation/Instability Signal Based on STI Equations of a Latent Variable  $v^t$ .** In addition to the unpredictability signal, we define another signal to detect the tipping point based on transition or bifurcation conditions. Based on the CSD principle (19), when the state of a system approaches a local bifurcation point (e.g., fold, Hopf, or transcritical bifurcation), its variation or fluctuation (e.g., SD) along the center manifold drastically increases due to the increased sensitivity to ubiquitous noise. Thus, provided that observations of the dynamics on the center manifold are available, a significant increase in the SD can be regarded as the fluctuation signal, the appearance of which indicates an upcoming abrupt transition of the system state.

We set  $v$  as the latent variable to detect the inconsistency signal by using Eq. 4. In addition to the weight matrices  $P$  and  $Q$ , all variables in the matrix of Eq. 1 are unknown and must be solved from the LV-STI equations. Since the latent variable  $v$  represents the dominant dynamics of the geodynamical system due to the transformation of the STI equations,  $v$  can be approximately viewed as a variable on the center manifold when the system approaches the tipping point for a generic local bifurcation (20). Then, the SD of the time series of  $v$  can be utilized to detect the fluctuation signal in a one-dimensional space. Specifically, the extended series  $\hat{v}^1 = (v^1, v^2, \dots, v^{m+L-1})'$  can be obtained by solving Eq. 4, yielding a time series of the SD, i.e.,  $\{SD(\hat{v}^1), SD(\hat{v}^2), \dots, SD(\hat{v}^{k-m+1}), \dots\}$ . For each time point  $t = k$ , if there is a significant difference between  $SD(\hat{v}^{k-m+1})$  and its precursors based on the one-sample  $t$  test, it is considered the fluctuation signal or the second type of an early-warning signal occurring at this time point. The details of solving the LV-STI equations are provided in *SI Appendix, Note S12*.

**The Sliding-Window Scheme of the Observed Time Series.** In this study, for the given real-time high-dimensional time series, RSIT was applied based on a sliding-window scheme. A sliding window  $w_k$  ranges from time point  $t = k$  to  $t = k + m - 1$ , i.e., the length of each sliding window is  $m$  (*SI Appendix, Fig. S10*). For each sliding window  $w_k$ , RSIT transforms the high-dimensional spatial information  $\mathbf{z}^t = (z_1^t, z_2^t, \dots, z_n^t)_{t=k, k+1, \dots, k+m-1}$  (the information of  $n$  variables) into the one-dimensional temporal information  $\hat{v}^k = (v^k, v^{k+1}, \dots, v^{k+m-1}, v^{k+m}, \dots, v^{k+m+L-2})'$  (the information of a target/latent variable  $v$ ). There are the following two parameters of sliding windows (*SI Appendix, Fig. S10*):

- $m$ , the length of the known short-term time series. It is also the size of a sliding window  $w_k$ .
- $L - 1$ , the length of to-be-extend future series for each sliding window  $w_k$ .

Besides, these two parameters together with the embedded neural networks including the number of layers, and the number of neurons were adjusted every year based on the most recent information (the information of last year in this study) with a line search-like strategy due to the time-varying geodynamics, as described in detail in *SI Appendix, Note S3*.

**RSIT Algorithm to Alert for Earthquakes.** The RSIT algorithm alerts for possible earthquakes based on both the fluctuation signal and the unpredictability signal via the following procedure.

1. Determining the earthquake-alerting signal: When a fluctuation/instability signal (FS) appears at time point  $t_{FS}$ , we set  $t_{FS}$  as the reference point. If an unpredictability/inconsistency signal (US) appears at time point  $t_{US}$  during a neighboring signal/time window  $SW_{neigh}$  around  $t_{FS}$ , i.e., before or after  $t_{FS}$ , then an

earthquake-alerting (EA) (or the RSIT signal) is provided at  $t_{EA} = \max(t_{FS}, t_{US})$  (Fig. 1D). The details of this step are illustrated in *SI Appendix, Fig. S11*.

2. Alerting for earthquakes based on warning signals: If an earthquake occurs at time point  $t_{EO}$  during a time window  $SW_{neigh}$  after  $t_{EA}$ , then a true earthquake-alerting signal is provided at  $t_{EA}$ .
3. Excluding postearthquake signals: RSIT discards signals appearing within a time window  $SW_{post-earthquake}$  after earthquake-occurring (EO) point  $t_{EO}$  when these signals represent a series of postearthquakes.

**Metrics for Evaluating the Earthquake-alerting performance.** A set of unified metrics is employed for evaluating the earthquake-alerting performance of any specific method as follows.

If an earthquake does occur at  $t_{EO}$  during a time window  $SW_{neigh}$  after  $t_{EA}$ , i.e.,  $t_{EO} - t_{EA} \leq SW_{neigh}$  (*SI Appendix, Fig. S11*), then the earthquake-alerting signal at  $t_{EA}$  is a true-positive (TP) alert; otherwise, it is a false-positive (FP) alert. Before an earthquake, if there is not any earthquake-alerting signal during a time window  $SW_{neigh}$  before  $t_{EO}$ , then it is a false-negative (FN) result; if there is neither an earthquake nor alerting signal during any window, then it is a true-negative (TN) result.

The detailed description of TP, FP, FN, and TN, as well as their calculation formula are provided in *SI Appendix, Note S5*. As successful early-warning cases presented in *SI Appendix, Fig. S12*, we demonstrate how successful alerts provide early-warning signals for imminent earthquakes.

**Existing Computational Methods for Performance Comparison.** Various time-series forecasting methods for earthquakes have been developed. To evaluate the earthquake alerting performance of RSIT, we compared it with the following existing ten methods. Among these previous methods, eight (methods M1–M8 below) are used specifically in geodetic science, while the other two (methods M9–M10 below) are employed more generally.

- Method 1 (M1) is a real-time outlier detection method based on a window-based forecasting model (49).
- Method 2 (M2) is a supervised machine learning algorithm designed for GNSS positioning time-series prediction (50).
- Method 3 (M3) is based on the definition of the randomness of outliers in GPS time series (51).
- Method 4 (M4) is the GPS Interactive Time Series Analysis (GITSAs) software program developed for the visualization and analysis of GPS time series in geodetic and geodynamic studies (52).
- Method 5 (M5) represents an ANN for predicting earthquakes using real-time GNSS data (15).
- Method 6 (M6) is a deep learning algorithm called WANEH that combines wavelets with neural networks and the Hilbert transform to detect anomalies in time-series data (53).
- Method 7 (M7) is a method based on martingale theory to extract anomalies from continuous GPS data as earthquake precursors (54).
- Method 8 (M8) represents a graphical method for detecting outliers in time series of continuous daily measurements (55).
- Method 9 (M9) represents support vector regression (SVR), a supervised machine learning algorithm (4).
- Method 10 (M10) is delayed long short-term memory (dLSTM), an anomaly detection method for time-series data (56).

The details of methods M1–M10 are provided in *SI Appendix, Note S14*. Besides, RSIT has been compared with the short-term seismicity-based models, such as the Epidemic Type Aftershock Sequence (ETAS) model (40, 41). The details are provided in *SI Appendix, Note S15 and Fig. S13*.

**Data, Materials, and Software Availability.** The raw GNSS data of prefectures of Japan were available from <https://www.jisinyosoku.com/> (58). The dataset of Sichuan, China was provided by Eastern Deformation Data Branch (<https://data.earthquake.cn/>) (59). The raw waveform data of Sichuan, China were accessible from <https://data.earthquake.cn/> upon request (60). The raw GNSS data of south-central Alaska, USA were available from <http://geodesy.unr.edu/> (61). The earthquake catalogue data of Japan and China were accessible from <http://www.data.jma.go.jp/svd/eqdb/data/shindo/index.html> (62) and <http://www.ceic.ac.cn/history> (63), respectively. The maps of GNSS monitoring stations in Japan were available from

<https://sokuseikagis1.gsi.go.jp/> (64). The maps of GNSS monitoring stations in Sichuan and south-central Alaska were available from <https://data.earthquake.cn/> and <http://geodesy.unr.edu/Acknowledgements.php> (61, 65), respectively. The code used in this study is available at <https://github.com/YuyanTong/RSIT> (66).

**ACKNOWLEDGMENTS.** This work was supported by the National Natural Science Foundation of China (Nos. 12322119, 62172164, 12271180, T2341007, T2350003, 31930022, and 12131020), the National Key R&D Program of China (No. 2022YFA1004800), the Strategic Priority Research Program of the Chinese Academy of Sciences (No. XDB38040400), Guangdong Provincial Key Laboratory of Human Digital Twin (No. 2022B1212010004), Major Key Project of PCL (No. PCL2021A12), JST Moonshot R&D Grant Number JPMJMS2021, AMED JP22dm0307009, and Institute of AI and Beyond at the University of Tokyo. The

1. P. Zhang *et al.*, Active tectonic blocks and strong earthquakes in the continent of China. *Sci. China, Ser. D Earth Sci.* **46**, 13–24 (2003).
2. V. Kaftan, A. Melnikov, Local deformation precursors of large earthquakes derived from GNSS observation data. *IOP Conf. Ser. Earth Environ. Sci.* **95**, 032030 (2017).
3. D. Thomas, Geochemical precursors to seismic activity. *Pure Appl. Geophys.* **126**, 241–266 (1988).
4. K. M. Asim, A. Idris, T. Iqbal, F. Martínez-Alvarez, Earthquake prediction model using support vector regressor and hybrid neural networks. *PLoS One* **13**, e0199004 (2018).
5. Z. Jilani, T. Mehmood, A. Alam, M. Awais, T. Iqbal, Monitoring and descriptive analysis of radon in relation to seismic activity of Northern Pakistan. *J. Environ. Radioact.* **172**, 43–51 (2017).
6. S. Pulinets, D. Ouzounov, Lithosphere–Atmosphere–Ionosphere Coupling (LAIC) model—An unified concept for earthquake precursors validation. *J. Asian Earth Sci.* **41**, 371–382 (2011).
7. R. D. Cicerone, J. E. Ebel, J. Britton, A systematic compilation of earthquake precursors. *Tectonophysics* **476**, 371–396 (2009).
8. T. Rikitake, Earthquake prediction. *Earth Sci. Rev.* **4**, 245–282 (1968).
9. S. Uyeda, K. S. Al-Damegh, E. Dologlou, T. Nagao, Some relationship between VAN seismic electric signals (SES) and earthquake parameters. *Tectonophysics* **304**, 41–55 (1999).
10. S. R. Mei, On the physical model of earthquake precursor fields and the mechanism of precursors' time-space distribution—Origin and evidences of the strong body earthquake-generating model. *Acta Seismol. Sin.* **8**, 337–349 (1995).
11. L. M. Jones, Foreshocks and time-dependent earthquake hazard assessment in southern California. *Bull. Seismol. Soc. Am.* **75**, 1669–1679 (1985).
12. P. A. Reasenberg, L. M. Jones, Earthquake hazard after a mainshock in California. *Science* **243**, 1173–1176 (1989).
13. J. L. Hardebeck, A. L. Llenos, A. J. Michael, M. T. Page, N. Van Der Elst, Updated California aftershock parameters. *Seismol. Res. Lett.* **90**, 262–270 (2019).
14. S. Narayanakumar, K. Raja, A BP artificial neural network model for earthquake magnitude prediction in Himalayas, India. *Circuits Syst.* **7**, 3456–3468 (2016).
15. M. Moustira, M. Avraamides, C. Christodoulou, Artificial neural networks for earthquake prediction using time series magnitude data or seismic electric signals. *Expert Syst. Appl.* **38**, 15032–15039 (2011).
16. Y. Hirata, K. Iwayama, K. Aihara, Possibility of short-term probabilistic forecasts for large earthquakes making good use of the limitations of existing catalogs. *Phys. Rev. E* **94**, 042217 (2016).
17. M. Kiani Possibility of land movement prediction for creep or before earthquake using Lidar Geodetic Data in a machine learning scheme. arXiv [Preprint] (2020). <https://arxiv.org/abs/2006.10419> (Accessed 6 May 2022).
18. C. Ito, H. Takahashi, M. Ohzono, Estimation of convergence boundary location and velocity between tectonic plates in northern Hokkaido inferred by GNSS velocity data. *Earth Planets Space* **71**, 1–8 (2019).
19. M. Scheffer *et al.*, Early-warning signals for critical transitions. *Nature* **461**, 53–59 (2009).
20. L. Chen, R. Liu, Z. P. Liu, M. Li, K. Aihara, Detecting early-warning signals for sudden deterioration of complex diseases by dynamical network biomarkers. *Sci. Rep.* **2**, 1–8 (2012).
21. F. Takens, "Detecting strange attractors in turbulence" in *Dynamical Systems and Turbulence, Warwick 1980*, D. Rand, L. S. Young, Eds. (Springer, 1981), pp. 366–381.
22. H. Ma, S. Leng, K. Aihara, W. Lin, L. Chen, Randomly distributed embedding making short-term high-dimensional data predictable. *Proc. Natl. Acad. Sci. U.S.A.* **115**, E9994–E10002 (2018).
23. P. Chen, R. Liu, K. Aihara, L. Chen, Autorenservoir computing for multistep ahead prediction based on the spatiotemporal information transformation. *Nat. Commun.* **11**, 1–15 (2020).
24. M. Ishida, "Seismicity and tectonics of Japan" in *Earthquakes and Seismotectonics of the Japanese Islands*, T. Hagiwara, Ed. (Kaijima Inst, 1989), pp. 57–85.
25. R. M. Musson "Intensity and intensity scales" in *IASPEI New Manual of Seismological Observatory Practice*, P. Bormann, Ed. (GeoForschungsZentrum, 2009), pp. 689–698.
26. D. R. Shelly, G. C. Beroza, H. Zhang, C. H. Thurber, S. Ide, High-resolution subduction zone seismicity and velocity structure beneath Ibaraki Prefecture, Japan. *J. Geophys. Res. Solid Earth* **111**, B06311 (2006).
27. Earthquake Research Committee, *Seismic Activity in Japan: Regional Perspectives on the Characteristics of Destructive Earthquakes* (Science and Technology Agency, 1998).
28. M. Tamaki, S. Kusumoto, Y. Itoh, Formation and deformation processes of late Paleogene sedimentary basins in southern central Hokkaido, Japan: Paleomagnetic and numerical modeling approach. *Isl. Arc* **19**, 243–258 (2010).
29. H. Lu *et al.*, CONET: A cognitive ocean network. *IEEE Wireless Commun.* **26**, 90–96 (2019).
30. X. Lei, J. Su, Z. Wang, Growing seismicity in the Sichuan Basin and its association with industrial activities. *Sci. China Earth Sci.* **63**, 1633–1660 (2020).
31. ChinaNetwork, *China Seismic Network Waveform Data* (China Earthquake Administration, 2006). 10.12001/ChinaNetwork.Data.
32. C. M. Handel, I. J. Stenhouse, *Alaska Landbird Conservation Plan—Version II* (Boreal Partners in Flight Working Group, Anchorage, AK, 2013), p. 18.
33. J. H. Hodgson, "Elementary seismology and seismic zoning" in *Proceedings of the Symposium on Earthquake Engineering* (The University of British Columbia, Vancouver, BC, Canada, 1966), pp. II-1–II-12.
34. R. Musson, The Barrow-in-Furness earthquake of 15 February 1865: Liquefaction from a very small magnitude event. *Pure Appl. Geophys.* **152**, 733–745 (1998).

waveform data were provided by the China Seismic Data Management Center at the Institute of Geophysics, China Earthquake Administration. We also thank the First Monitoring and Application Center, China Earthquake Administration for providing the GNSS velocity field datasets/ time series of GPS stations.

Author affiliations: <sup>a</sup>School of Mathematics, South China University of Technology, Guangzhou 510640, China; <sup>b</sup>Key Laboratory of Systems Health Science of Zhejiang Province, Hangzhou Institute for Advanced Study, University of Chinese Academy of Sciences, Chinese Academy of Sciences, Hangzhou 310024, China; <sup>c</sup>International Research Center for Neurointelligence, The University of Tokyo Institutes for Advanced Study, The University of Tokyo, Tokyo 113-0033, Japan; <sup>d</sup>Key Laboratory of Systems Biology, Shanghai Institute of Biochemistry and Cell Biology, Center for Excellence in Molecular Cell Science, Chinese Academy of Sciences, Shanghai 200031, China; <sup>e</sup>Guangdong Institute of Intelligence Science and Technology, Hengqin, Zhuhai, Guangdong 519031, China; and <sup>f</sup>School of Life Science and Technology, ShanghaiTech University, Shanghai 201210, China

35. M. R. Lamsal, Seismic activity and its periphery. *Himal. Phys.* **6**, 86–91 (2017).
36. N. Das, R. Bhandari, D. Ghose, P. Sen, B. Sinha, Significant anomalies of helium, radon and gamma ahead of 7.9 M China earthquake. *Acta Geod. Geophys.* **44**, 357–365 (2009).
37. R. Westaway, N. M. Burnside, Fault "corrosion" by fluid injection: A potential cause of the November 2017 M<sub>w</sub> 5.5 Korean Earthquake. *Geofluids* **2019**, 1280721 (2019).
38. R. Westaway, P. L. Younger, Quantification of potential macroseismic effects of the induced seismicity that might result from hydraulic fracturing for shale gas exploitation in the UK. *Q. J. Eng. Geol. Hydrogeol.* **47**, 333–350 (2014).
39. R. P. Dhakal, T.-C. Pan, Response characteristics of structures subjected to blasting-induced ground motion. *Int. J. Impact Eng.* **28**, 813–828 (2003).
40. R. Geller, D. Jackson, Y. Kagan, F. Mulargia, Earthquakes cannot be predicted. *Science*, **275**, 1616–1616 (1997).
41. Y. Ogata, Statistical models for earthquake occurrences and residual analysis for point processes. *J. Am. Stat. Assoc.* **83**, 9–27 (1988).
42. T. Omi, Y. Ogata, Y. Hirata, K. Aihara, Estimating the ETAS model from an early aftershock sequence. *Geophys. Res. Lett.* **41**, 850–857 (2014).
43. M. C. Gerstenberger, S. Wiemer, L. M. Jones, P. A. Reasenberg, Real-time forecasts of tomorrow's earthquakes in California. *Nature* **435**, 328–331 (2005).
44. A. J. Michael, M. J. Werner, Preface to the focus section on the Collaboratory for the Study of Earthquake Predictability (CSEP): New results and future directions. *Seismol. Res. Lett.* **89**, 1226–1228 (2018).
45. T. Sauer, J. A. Yorke, M. Casdagli, Embedology. *J. Stat. Phys.* **65**, 579–616 (1991).
46. R. Tao, T. Lu, Y. Cheng, X. He, X. Wang, "An improved GNSS vertical time series prediction model using EWT" in *China Satellite Navigation Conference (CSNC 2021) Proceedings*, C. Yang, J. Xie, Eds. (Springer Singapore, 2021), pp. 298–313.
47. G. B. Huang, Q. Y. Zhu, C. K. Siew, Extreme learning machine: Theory and applications. *Neurocomputing* **70**, 489–501 (2006).
48. V. De Rubéis, Z. Czechowski, R. Teisseyre, Eds., *Synchronization and Triggering: From Fracture to Earthquake Processes* (Springer, 2010).
49. A. V. Klyuchevskii, Nonlinear geodynamics of the Baikal Rift System: An evolution scenario with triple equilibrium bifurcation. *J. Geodyn.* **49**, 19–23 (2010).
50. Y. Yu, Y. Zhu, S. Li, D. Wan, Time series outlier detection based on sliding window prediction. *Math. Probl. Eng.* **2014** (2014).
51. M. Kiani A specifically designed machine learning algorithm for GNSS position time series prediction and its applications in outlier and anomaly detection and earthquake prediction. arXiv [Preprint] (2020). <https://arxiv.org/abs/2006.09067> (Accessed 1 May 2022).
52. A. Lyubushin, P. Yakovlev, Entropy measure of stepwise component in GPS time series. *Izv. Phys. Solid Earth* **52**, 96–104 (2016).
53. M. A. Goudarzi, M. Cocard, R. Santerre, T. Woldai, GPS interactive time series analysis software. *GPS Solut.* **17**, 595–603 (2013).
54. S. Kanarachos, S. R. G. Christopoulos, A. Chronos, M. E. Fitzpatrick, Detecting anomalies in time series data via a deep learning algorithm combining wavelets, neural networks and Hilbert transform. *Expert Syst. Appl.* **85**, 292–304 (2017).
55. N. Li, X. Kong, L. Lin, Anomalies in continuous GPS data as precursors of 15 large earthquakes in Western North America during 2007–2016. *Earth Sci. Inf.* **13**, 163–174 (2020).
56. D. Arabelos *et al.*, The use of an outlier detecting method in time series of continuous daily measurements of underground water level and temperature in earthquake prediction investigation. *Tectonophysics* **338**, 315–323 (2001).
57. S. Maya, K. Ueno, T. Nishikawa, dLSTM: A new approach for anomaly detection using deep learning with delayed prediction. *Int. J. Data Sci. Anal.* **8**, 137–164 (2019).
58. Y. Ohta, GNSS continuous observation system elevation data. GPS crustal deformation observations and earthquake prediction. <https://www.jisinyosoku.com/>. Accessed 1 March 2022.
59. The First Monitoring and Application Center, China Earthquake Administration. GNSS time series of GPS stations. <https://data.earthquake.cn/>. Accessed 18 March 2022.
60. China Earthquake Networks Center, National Earthquake Data Center. China Seismic Network waveform data. <https://data.earthquake.cn/>. Accessed 18 March 2022.
61. G. Blewitt, B. Hammond, C. Kreemer, Nevada Geodetic Laboratory. GPS timeseries data. <http://geodesy.unr.edu/index.php>. Accessed 18 March 2022.
62. Japan Meteorological Agency, The seismic intensity database. <https://www.jma.go.jp/jma/index.html>. Accessed 18 March 2022.
63. China Earthquake Network Center, Earthquake catalogue data. <http://www.ceic.ac.cn/history>. Accessed 18 March 2022.
64. Geospatial Information Authority of Japan, The maps of GNSS monitoring stations. <https://sokuseikagis1.gsi.go.jp/>. Accessed 18 March 2022.
65. U.S. Geological Survey, Earthquake Lists, Maps, and Statistics. <https://www.usgs.gov/natural-hazards/earthquake-hazards/lists-maps-and-statistics>. Accessed 18 March 2022.
66. Y. Tong *et al.*, RSIT. GitHub. <https://github.com/YuyanTong/RSIT>. Deposited 15 February 2023.